Energy Storage Materials 90 (2026) 105409

Contents lists available at ScienceDirect

Energy Storage Materials

journal homepage: www.elsevier.com/locate/ensm

Electrochemical activity and utilization in iron-air batteries governed by grain size

Adam Cohen Miles [a,*], Yujun Zhao [a], Dierk Raabe [a], Yan Ma [a,b,*], Yug Joshi [a,*]

[a] Max Planck Institute for Sustainable Materials, Max Planck Str. 1, 40237, Düsseldorf, Germany
[b] Department of Materials Science & Engineering, Delft University of Technology, Mekelweg 2, Delft, 2628 CD, The Netherlands

ARTICLE INFO

Keywords:
Iron-air battery
Grain boundaries
Microstructure
Energy storage
Grid storage
Metal air battery

ABSTRACT

Iron-air batteries are re-emerging as cost-effective and sustainable candidates for long-duration energy storage. The anode performance is often improved by maximising surface area via morphological changes or introducing chemical additives. Here we investigate the inherent role of the anode's microstructure in the electrochemical activity. We isolate the effect of grain size, and thus grain boundary density, on the electrochemical behavior of high-purity iron anodes by eliminating confounding factors such as porosity, dopants, and additives. A strong inverse correlation between grain size and electrochemical performance is observed, with ultrafine-grained anodes (ca. 1 μm) exhibiting up to 50-fold higher current densities than coarse-grained counterparts (ca. 2500 μm). Kinetic analysis revealed a strong transition of fluxes from an interfacial-controlled toward a diffusion-controlled regime upon reduction of grain sizes. Post-cycling characterization shows that the reaction remains spatially confined due to oxide formation, limiting the electrochemically accessible fraction of the electrode. Grain refinement enhances transport pathways, enabling deeper reaction penetration and increasing the accessible fraction of iron. These findings establish grain size as a governing microstructural parameter controlling transport, reaction accessibility, and utilization in iron-air systems.

1. Introduction

Grid-scale energy storage solutions are an attractive strategy to overcome the high intermittency of sustainable energy. Long-duration energy storage (10–100 h) is necessary to balance the discrepancy between the energy demand and renewable energy generation [1,2]. Currently, vanadium redox flow batteries (VRFB) dominate grid-scale storage because of their excellent durability, exceeding 10,000–20,000 charge-discharge cycles. However, their broader deployment is constrained by the volatile pricing and geographically concentrated supply of vanadium. Currently, over 60% of global production of vanadium originates from China and the remainder primarily from Russia, South Africa, and Brazil [3]. Additionally, VRFBs suffer from low energy density of 15–25 Wh/L and 10–35 Wh/kg, substantially lower than competing technologies [4–6]. Zinc-air batteries offer notable safety and cost advantages for stationary applications. However, they often suffer from limited cycle life, typically around 150 cycles for solid-state designs and up to 600 h for optimized systems at low depth-of-discharge. In addition, electrode degradation remains a significant challenge, restricting long-term performance and commercial reliability [7–9]. Recently, iron-air batteries have re-emerged as a promising candidate for large-scale energy storage, leveraging the abundance of iron (5.6% of Earth's crust by mass, the fourth most abundant element). Moreover, it offers unparalleled environmental sustainability due to the high level of recyclability of iron [10]. Additionally, they deliver a competitive theoretical energy density exceeding 1200 Wh/kg. In contrast, lithium-based alternatives suffer from supply chain issues and safety hazards [11–15]. System studies and techno-economic analyses indicate that discharge durations of 10 to 100 h (for multi-day applications) require a specific energy of about 50 to 75 $Wh \bullet kg^{-1}$ [16–18]. Given these requirements, iron-air concepts have been identified as promising candidates for low cost, multi day storage [19,20].

The exact redox reaction is still under debate, with reports discussing the formation of $Fe(OH)_2$, which can further oxidize to FeOOH or $Fe(OH)_3$ or Fe_3O_4 followed by γ-Fe_2O_3 [21–23]. This is most-likely due to the localized variation of pH and sensitivity of the reaction products towards the pH [24]. Nevertheless, currently the iron-air battery research primarily explores improving anode performance via maximizing the surface-to-volume ratio. This is commonly achieved by using iron-based nanoparticles and highly porous architectures. These

* Corresponding authors.
E-mail addresses: a.miles@mpi-susmat.de (A.C. Miles), yan.ma@tudelft.nl (Y. Ma), y.joshi@mpi-susmat.de (Y. Joshi).

https://doi.org/10.1016/j.ensm.2026.105409
Received 15 April 2026; Received in revised form 23 June 2026; Accepted 23 July 2026
Available online 24 July 2026

structures enhance electrochemical activity and cyclability by shortening diffusion pathways [11,25,26]. In parallel to morphological approaches, chemical modification has also been explored by incorporating additives (as dopants or electrolyte additive) such as FeS, FeS_2, Bi_2S_3, Bi_2O_3, Na_2S, K_2S. The additives impede the parasitic hydrogen evolution reaction (HER) and promote the overall anode longevity by preventing passivation [27–30], which occurs when iron forms an insulating, irreversible Fe_3O_4 or γ-Fe_2O_3 layer that isolates the underlying bulk metal from the electrolyte [23].

While such structural architecting and chemical modification approaches have yielded significant advances for iron-air technology, they do not isolate the intrinsic role of iron microstructure, leaving a critical gap in the understanding of iron-air anode behavior. Generally, microstructure can directly impact electrochemical behavior. For example, grain boundaries can serve as fast diffusion pathways for ionic transport, thus influencing the spatial distribution of charge transfer reactions and current density [31–35].

To understand these microstructural contributions better, Fig. 1a illustrates the hydroxide-ion based transport that governs the iron-air battery operation. The inset figure highlights that grain boundaries can act as preferential high-mobility transport pathways for the formation and dissolution of intermediate Fe hydroxide and Fe oxide phases. In this representation, the accessibility of the bulk iron is determined not only by the intrinsic chemistry but also by the microstructure of the metal. Fig. 1b–d show a simplified scaling model to quantify how iron anode utilization and inactive cell mass affect the practical energy density and cost of iron-air batteries, (explained in detail in supplementary note 1). Fig. 1b illustrates the linear dependence of system energy density with the anode utilization across a representative range of iron mass fractions (f) in the total battery. The mass fraction, f is defined as the mass of iron divided by the total battery mass. f ranges from 0.10 to 0.15 for fully submerged configurations, it corresponds to 0.18 for more compact solid-state high loading designs, and extends up to 0.20 as an upper bound estimate used in theoretical system-level analyses [13,22]. It is clear from the figure (see red arrow) that even a modest increase in utilization shifts the system from subthreshold performance into the regime above a practical target of roughly 50 Wh•kg^{-1} [17,18]. A similar trend is observed in the cost projections shown in Fig. 1c, where the specific cost decreases strongly with increasing utilization and remains well below the widely accepted ~$100 kWh^{-1} system-level cost threshold for economically viable long-duration energy storage [36]. When energy density and cost are considered simultaneously, as shown in Fig. 1d, a performance window emerges, highlighted in green, in which iron-air batteries become competitive at grid scale. The motivation presented clearly indicates that entry into this regime is governed by anode utilization. Enhancing utilization thus becomes a central objective, prompting strategies that go beyond electrode structuring and porosity to include targeted modifications of the iron microstructure as an alternative approach.

This study aims to understand the effect of iron anode's

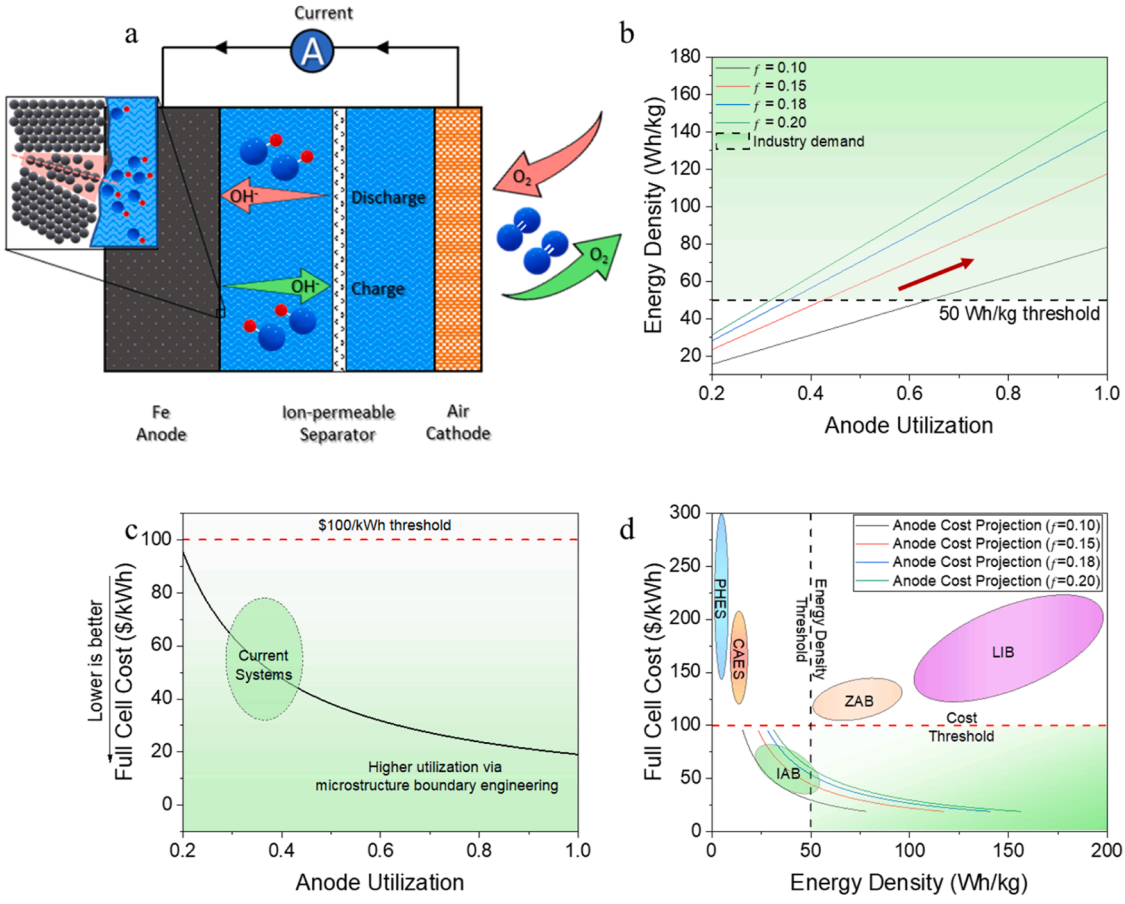

Fig. 1. a) Schematic illustration of the electrochemical reactions in an aqueous iron-air battery, emphasizing the role of grain boundaries as potential channels that facilitate the interconversion between Fe, $Fe(OH)_2$, and Fe_3O_4/FeOOH species. b) Calculated dependence of overall energy density on anode utilization for different Fe mass fractions within the cell, indicating that only high utilization levels enable Fe–air systems to surpass the practical 50 Wh kg^{-1} threshold required for large-scale energy storage. c) Specific cost projection as a function of Fe utilization, highlighting the steep decrease in cost with improved utilization and the resulting flexibility for additional expenses associated with microstructural optimization. d) Comparative plot of system-level energy density versus full-cell cost, demonstrating that with sufficient Fe utilization, both cost and energy density targets can be simultaneously achieved, positioning Fe–air technology as a competitive long-duration energy storage solution.

microstructure, particularly grain size, on the electrochemical activity. Particular attention is paid to eliminate the effect of factors like porosity, tortuosity, dopants, and additives. Thus, planar polished electrodes with various grain sizes were investigated. The study demonstrates a strong inverse relationship between grain size and electrochemical performance. The electrodes with a grain size of ca. 1 μm show redox peaks exceeding 8.8 mA•cm^{-2}, which is about 2.5 times higher compared with 20 μm grain-sized electrodes. Moreover, a shift in the diffusive current contribution from about 16% to nearly 60% upon such grain size reduction. This increase in diffusive current contribution is rationalized by ca. 20 times increase in the apparent diffusion coefficient upon a grain-size reduction from ca. 20 μm to 1 μm. The study therefore confirms that grain boundary density will directly influence the kinetics of phase conversion and will govern the accessible reaction depth or anode utilization in the iron-air system.

2. Results and discussion

2.1. Effect of microstructure on redox-activity

To investigate the intrinsic influence of grain size on iron redox behavior, a three-electrode configuration was employed, as shown in Fig. 2a (see also Experimental section). Pt mesh counter electrode and a reversible hydrogen electrode (RHE) were used as counter (CE) and reference electrode (RE), respectively. Fe plates (>99.99%) served as working electrodes and were annealed to obtain the target grain sizes, followed by identical grinding and polishing procedures for all microstructural states, as described in the Experimental Section and shown in Fig. S1. The Fe samples were installed in an electrode holder with a fixed 6 mm circular aperture, ensuring the same geometric electrode area across the samples. Moreover, careful macroscopic surface preparation ensured no surface morphological differences among the samples with different grain sizes, i.e., no differences in porosity, chemical composition, and surface roughness. These measures allowed the observed electrochemical differences to be attributed primarily to differences in grain size and grain boundary density.

The microstructures prepared for this study are shown in Fig. 2b–d. Grain sizes were tuned through controlled heat treatments to produce three distinct states: a quasi-single-crystal (ca. 2500 μm grain size), a coarse-grained sample (ca. 20 μm grain size), and a fine-grained sample (ca. 1 μm grain size). The grain-size analysis via Electron backscatter diffraction (EBSD) mapping is shown in Fig. S2. These samples are referred to as Fe2500, Fe20, and Fe01, respectively, hereafter. Moreover, EBSD further confirmed a crystalline structure of body-centered cubic (BCC) Fe.

The electrochemical performance of the samples was determined using cyclic voltammetry (CV). Fig. 2e–g show the representative cyclic voltammograms collected during the first cycle at 100 mV/s in 6 M KOH. Surprisingly, the Fe2500 sample exhibits almost no discernible redox response, with peak currents of mere ca. 0.17 mA•cm^{-2} as shown in the inset in Fig. 2e. Fe20 shows moderate activity, with oxidation and reduction peaks reaching ca. 3.54 mA•cm^{-2}. In contrast, the fine-grained sample displayed the expected well-defined, high-intensity peaks exceeding ca. 8.84 mA•cm^{-2}. The associated reactions or the changes in the oxidation states of Fe are highlighted in Fig. 2f and g

2.2. Phase transformations during redox cycles

The post-mortem characterization of the Fe01 electrodes after 100 cycles is shown in Fig. 3 (additional SEM images can be found in Fig. S4). Fig. 3a and b show the scanning electron microscope (SEM) image of overall reaction zone and a magnified region (marked by a red magnifying glass in Fig. 3a), respectively. The circular reaction zone appears darker than the unreacted zone in Fig. 3a. A closer inspection in Fig. 3b shows the appearance of small nodules or circular particles with size ranging between ca. 200–500 nm in diameter. The transmission electron microscopy (TEM) image of such particles is shown in the inset in Fig. 3c. The corresponding azimuthally averaged selected area diffraction pattern (SAED) confirms the presence of spinel-like crystal structure (Fd$\bar{3}$m) (see also Fig. S3 in supplementary information for raw data). This is either magnetite (Fe_3O_4) or maghemite (γ-Fe_2O_3 or $Fe_{2.67}O_4$), as the diffraction patterns for both only differ from an insignificant shift in reflections. The existence of the γ-Fe_2O_3 phase in the context of iron-air anode passivation has been confirmed in prior works using Raman spectroscopy [23,37], so the nodules are either purely γ-Fe_2O_3 or most-likely a mixture of Fe_3O_4 and its cation-deficient counterpart i.e.,

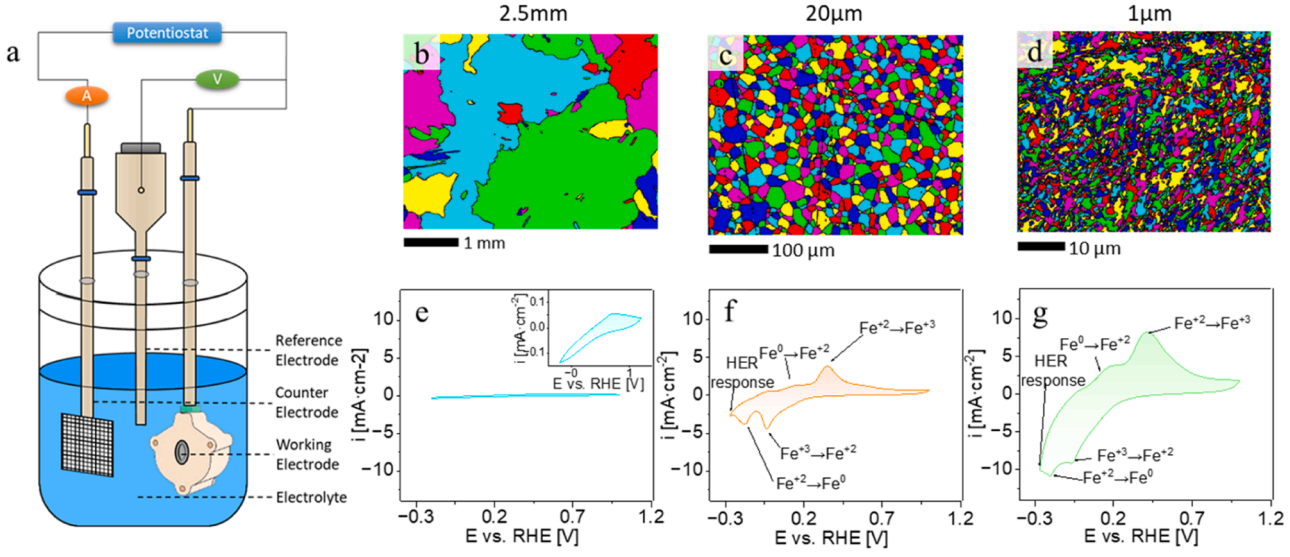

Fig. 2. Direct effect of grain size of Fe on electrochemical reduction/oxidation activity. a) Schematic illustration of the three-electrode electrochemical cell, comprised of a polyether ether ketone (PEEK) electrode holder with a 6 mm circular window, Pt-mesh counter electrode and an RHE reference electrode, all housed in an in-house made Teflon vessel equipped with holes for each electrode. b-d) Electron backscatter diffraction (EBSD) grain maps of Fe2500 (2.5 mm), coarse-grained Fe20 (20 μm), and fine-grained Fe01 (1 μm) iron samples. e-g) Cyclic voltammograms of all three samples at 100 mV/s in 6 M KOH, demonstrating progressive enhancement of redox activity with decreasing grain size. The inset in e) shows magnified view highlighting the negligible electrochemical activity of the Fe2500 sample.

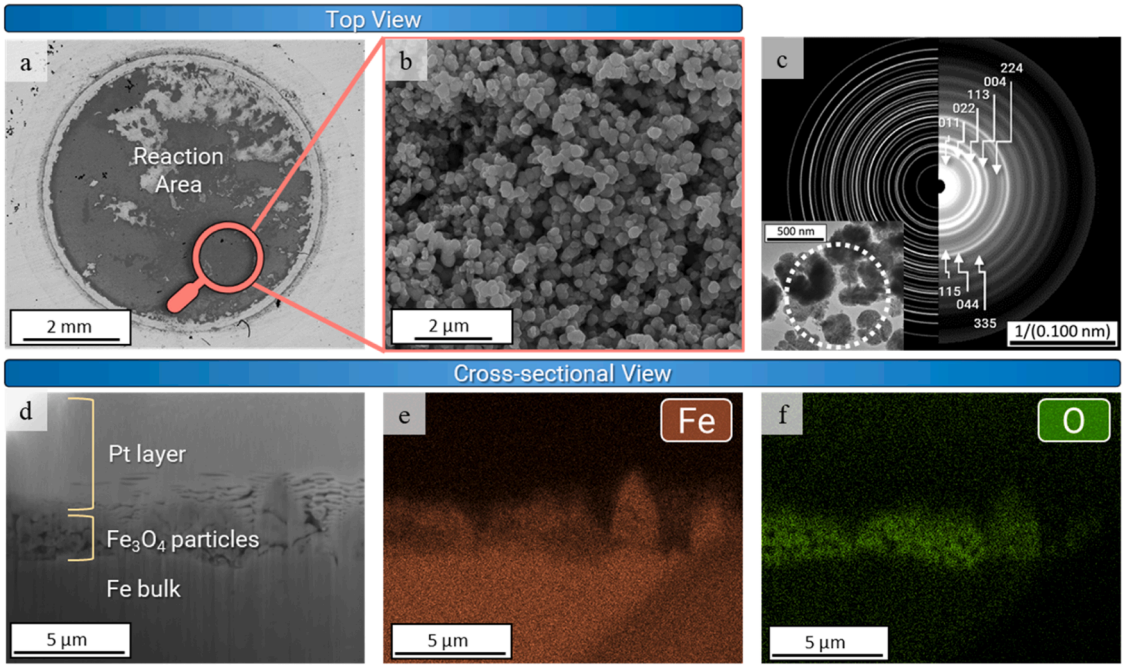

Fig. 3. Post mortem structural and compositional characterization of the Fe01 iron electrode after electrochemical cycling. (a) Top view secondary electron (SE) SEM image showing the electrode surface, where the circular region inside the aperture corresponds to the electrochemically cycled reaction area, while the surrounding surface remains uncycled. (b) Higher magnification SE SEM image of the cycled region, revealing a dense coverage of nanoparticles formed during cycling. (c) Transmission electron microscopy (TEM) analysis of the particles, including an azimuthally averaged selected area electron diffraction pattern obtained from the cycled surface and a calculated reference pattern for magnetite (Fe_3O_4), demonstrates agreement and confirms the polycrystalline magnetite nature of the particles. The inset shows a bright-field TEM micrograph of representative particles. (d) Cross-sectional SE SEM image of the same electrode prepared by focused ion beam milling, showing the bulk iron substrate, an overlying layer of magnetite particles, and a protective platinum layer deposited prior to ion milling. (e,f) Energy dispersive X-ray spectroscopy elemental maps of iron and oxygen, respectively, confirming the spatial separation between the metallic iron bulk and the oxygen rich oxide layer formed during cycling.

γ-Fe_2O_3 or $Fe_{2.67}O_4$

To determine the distribution of the spinel phase on the electrode's surface layer, a cross-section of the cycled electrode was taken in Fig. 3d The corresponding energy dispersive X-ray spectroscopy (EDX) taken from the cross-section are shown in Fig. 3e and 3f. The results suggest that (i) the complete electrode does not participate in the Fe redox reaction and (ii) the redox reaction is not fully reversible, as the residual spinel exists even though the sample was recovered under open-circuit voltage (OCV) condition of a pure Fe electrode.

To further probe the electrochemical consequences of this surface transformation, the cyclic voltammograms of the Fe01 electrode before and after extended cycling were compared, as shown in Fig. S5. After 100 cycles, the oxidation current was substantially suppressed and the redox features became broader, indicating a progressive loss of electrochemically accessible iron during cycling. This trend is consistent with the double-layer capacitance analysis performed using non-faradaic CVs for pristine and cycled samples, as shown in Fig. S6. The extracted capacitances were $C_{dl,pristine}$=1.69 mF•cm^{-2} and $C_{dl,cycled}$=0.51 mF•cm^{-2}, reflecting a decrease of 70.25% in double layer capacitance. This can be directly linked to the spinel-type oxide particles, which mask active Fe species from the electrode/electrolyte interfaces and reduce the electrochemically active area, hence reducing the total capacitance upon cycling.

The suppressed oxidation current after 100 cycles, together with the decrease in double-layer capacitance, indicates that the oxide layer not only remains as a passive reaction product but also limits subsequent redox reactions at the anode interface. Beyond serving as a marker of incomplete reversibility, this oxide layer introduces an additional transport barrier that limits ionic and electronic accessibility to the underlying iron. As a result, the progression of the reaction front into the bulk is restricted, leading to a reduced electrochemically accessible fraction of the electrode.

As shown in Fig. S4, the surface morphology after 100 electrochemical cycles varies markedly with grain size. Under these cycling conditions, the planar electrodes remain macroscopically intact, but their surfaces undergo microstructure-dependent passivation. Fe2500 shows no readily visible surface oxide formation under the applied SEM imaging conditions and is morphologically least altered, but it also exhibits weak electrochemical response. Fe20 exhibits finer and less geometrically uniform oxide features, whereas Fe01 shows denser coverage of more geometrically developed nodular oxide particles. These observations indicate that repeated redox cycling produces a trade-off between surface stability and electrochemical activity: the morphologically least altered surface is not necessarily the most active, while the enhanced activity of finer-grained iron is accompanied by stronger surface oxide formation.

2.3. *Kinetic implications of grain boundary density*

This raises the question of whether the enhanced activity in Fe01 is governed by surface-controlled processes or by transport limitations. Improved transport would enable deeper reaction penetration and increase the electrochemically accessible fraction of the material.

From the above results, it is evident that the reaction kinetics are governed by the microstructure. To quantitatively rationalize these effects and to further distinguish between surface- and diffusion-controlled contribution, scan-rate dependent CV was performed on samples Fe20 and Fe01. Fig. 4a clearly shows that across scan rates from 5 to 100 mV/s, the Fe01 (solid lines) material consistently exhibits higher current densities and sharper redox features compared with Fe20 (dashed line). Dunn's analysis was performed to distinguish the capacitive contributions (surface charge storage or pseudocapacitive) from

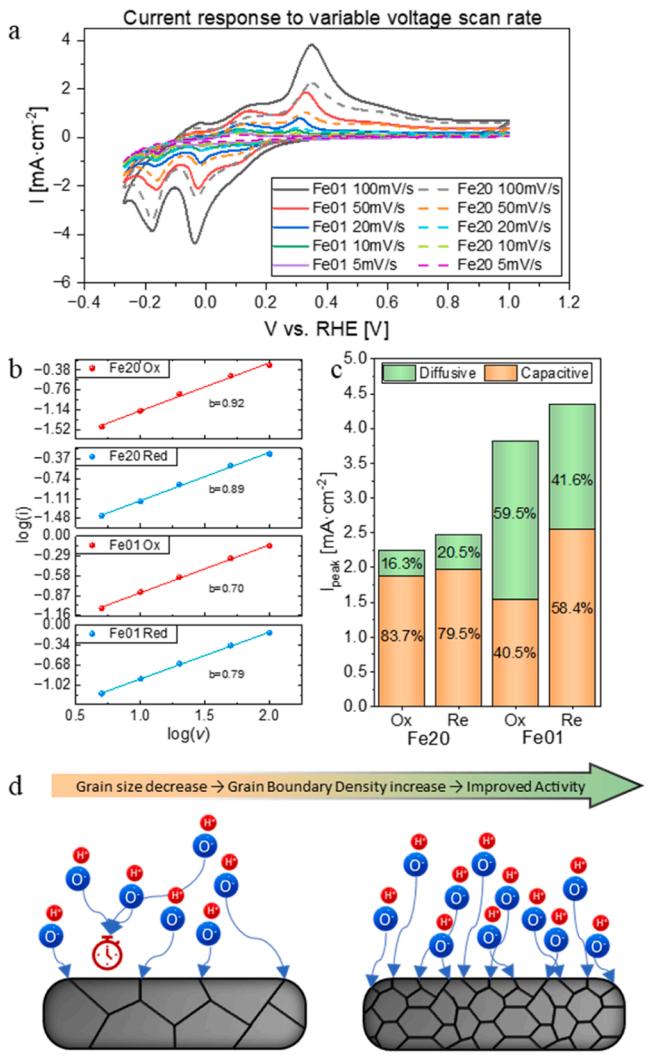

Fig. 4. Impact of grain boundary density on capacitive and diffusive charge storage. a) Cyclic voltammograms of coarse-grained (20 μm) and fine-grained (1 μm) iron samples collected in 6 M KOH at scan rates from 5 to 100 mV/s, demonstrating enhanced electrochemical activity with decreasing grain size across all scan rates. b) Dunn analysis, showing linear fits of peak current versus scan rate for the last oxidation and first reduction processes (Fe^{3+}/Fe^{2+} interconversion). c) Absolute capacitive and diffusion-controlled current contributions at 100 mV s^{-1} for Fe20 and Fe01, showing that grain refinement increases both the diffusion-controlled fraction and the total current response. d) Schematic illustration of the mechanistic importance of grain boundaries (GB), comparing two samples with contrasting GB densities and their effect on charge storage.

diffusive ones [38,39]. The total contribution of the current density can be described as:

$$i_p = a\nu^b \tag{1}$$

Where a and b are adjustable parameters, having contributions from diffusion, surface concentration, diffusion depth, etc. [40,41]. At the extreme ends, the value of $b = 0.5$ and $b = 1.0$ corresponds to a diffusion-controlled regime and the surface-controlled reaction (or capacitive behavior), respectively.

The Fe20 sample exhibits a higher slope, indicating a larger capacitive contribution in the coarse-grained material. The relative contributions of capacitive and diffusion-controlled processes are summarized in Fig. 4c. The Fe01 sample exhibits a significantly higher diffusion-controlled contribution during the Fe(II) to Fe(III) transition, reaching 59.5%, compared with only 16.3% for Fe20 under identical conditions. This demonstrates a clear shift toward diffusion-governed electrochemical behavior with decreasing grain size.

Importantly, this shift is accompanied by a substantial increase in the absolute current response. When expressed in absolute terms at a representative scan rate of 100 mV s^{-1}, both the capacitive and diffusion-controlled contributions increase significantly with decreasing grain size. The same qualitative trend is observed across the full scan-rate range; 100 mV s^{-1} is shown here as a representative condition where the redox features are clearly resolved and direct comparison between microstructures is straightforward.

These results indicate that grain refinement does not merely alter the dominant charge storage mechanism, but also increases the total electrochemically active response. The higher diffusion-controlled current observed in Fe01 therefore reflects not only enhanced transport kinetics, but also a larger electrochemically accessible fraction of iron.

2.4. Diffusion coefficient evaluation

The increased diffusion-controlled contributions observed for the fine-grained Fe01 sample indicate that transport processes play a dominant role in governing the electrochemical response. Since the diffusion-controlled current directly reflects the rate of species transport within the electrode, it provides a quantitative basis for evaluating the underlying transport properties. To further quantify these effects, the apparent diffusion coefficients (microstructurally averaged) were extracted from the diffusion-controlled peak currents using the Randles-Sevcik relation (see Experimental section) [42] and are displayed in Table 1. These values fall within the range reported for solid-state and defect-mediated transport in Fe hydroxides and oxyhydroxides at room temperature, typically between 10^{-12} and 10^{-17} $cm^2 \bullet s^{-1}$, depending on structure, hydration, and microstructural state [43,44]. A nearly twenty times difference in diffusivity between the Fe01 and Fe20 reflects the significant role of grain boundaries as fast transport pathways that increases the accessibility of redox sites.

3. Perspectives and practical implications for battery design

While the apparent diffusion coefficients were extracted from CV, their implications extend far beyond the timescale of a voltammetric sweep. In an operational iron-air system, the rate at which the Fe conversion front can advance into the particle governs how much of the iron is participating during cycling. The diffusion coefficients calculated in this work provide a quantitative measure of this progression. Even though the absolute timescale of voltammetry does not match that of a practical battery or energy storage device, the relative differences in apparent diffusivity between microstructures translate directly into differences in achievable reaction depth during sustained cycling.

For the fine-grained Fe01 sample, the higher apparent diffusivity values indicate that the redox reaction proceeds at a rate capable of accessing regions far from the particle surface over a typical discharge period. In a multi-hour or multi-day discharge profile characteristic of long-duration iron-air systems, this increased ion mobility allows the reaction to penetrate more deeply into each particle and engage a larger fraction of the stored iron. As a result, more of the active mass participates in the Fe-based conversion reaction. This directly improves the electrochemically accessible fraction and, consequently, the effective utilization of the active material and reduces the amount of unused material. Lastly, it should be pointed out that while both Fe01 and Fe20 did show the formation of the irreversible nodules (most-likely of Fe_3O_4 or $Fe_{2.67}O_4$), these were not apparent in the Fe2500 (see SI S4). This may point to the effect of GB density on the nucleation of such phases. The nucleation, texture, and strain also most likely contribute to the kinetics of the redox reaction; these are currently beyond the scope of the present work and will be focused on in the future.

The current findings unravel the critical role of grain boundaries in controlling ion transport in iron-air redox processes. In microstructures

Table 1
Kinetic parameters extracted from scan rate dependent cyclic voltammetry for fine grained and coarse-grained iron samples. Values of K1, K2, and the resulting apparent diffusion coefficients show the pronounced increase in diffusion-controlled contributions for the 1 μm finer microstructure.

Grain Size [μm]	Reduction			Oxidation		
	K1 $\left[\frac{mA}{mV/s}\right]$	K2 $\left[\frac{mA}{\sqrt{mV/s}}\right]$	D_{app} $\left[\frac{cm^2}{s}\right]$	K1 $\left[\frac{mA}{mV/s}\right]$	K2 $\left[\frac{mA}{\sqrt{mV/s}}\right]$	D_{app} $\left[\frac{cm^2}{s}\right]$
1	−0.00489	−0.02554	1.30×10^{-14}	0.00406	0.03466	2.40×10^{-14}
20	−0.00469	−0.00816	1.33×10^{-15}	0.00481	0.0077	1.20×10^{-15}

with low grain boundary density, the reaction is confined to isolated surface sites and relies on relatively long-distance transport of O species, which is known to be slow in alkaline environments [45]. In microstructures with high boundary density, a connected network of fast diffusion paths is introduced, which facilitates rapid movement of ions and electrons and accelerates the progression of the redox front. This mechanism is schematically illustrated in Fig. 4d A finer grain structure therefore not only increases the number of kinetically active sites but also improves the ability of the electrode to accommodate diffusion-controlled processes. At the same time, grain refinement introduces an important design trade-off. Although smaller grains improve current density and reaction accessibility, the increased grain-boundary density may also promote oxide nucleation and accelerate degradation during repeated cycling. Therefore, simply decreasing grain size is unlikely to provide a universal long-term improvement. Instead, grain size should be treated as one of the vital components of an integrated electrode design strategy, which should also include porosity, tortuosity, mass loading, and additives. All these parameters balance the (i) reaction accessibility (or total diffusion length); (ii) transport kinetics (enhanced via GB transport); and (iii) passivation control in iron-air anodes (by having either a very high surface area or the addition of additives to limit the formation or make them electrochemically active).

4. Conclusion

This work establishes that the electrochemical activity of iron anodes in alkaline iron-air systems is strongly governed by the microstructure. A decrease in grain size results in pronounced enhancements in redox activity. Fine-grained iron exhibits substantially higher current densities, increased grain-boundary-mediated charge transfer, and markedly larger diffusion-controlled contributions compared with coarse-grained and quasi-single-crystal counterparts. Post-cycling characterization reveals the formation of spinel-type oxide phases at the electrode surface, which correlates with a significant reduction in double-layer capacitance and indicates partial loss of electrochemically accessible surface area during cycling. Despite this phase transformation at the surface, fine-grained iron maintains superior transport kinetics, reflected in apparent diffusion coefficients nearly an order of magnitude higher than those of coarser microstructures.

For practical iron-air anode design, these findings suggest that grain size should be optimized together with electrode thickness and architecture. In thick or high-mass-loading electrodes, particles with finer internal grain structures may help reduce the fraction of inactive iron buried in the bulk by providing faster transport pathways along the grain boundary and hence allowing the reaction front to penetrate more deeply into the anode material. While porosity and tortuosity govern electrolyte access at the electrode scale, the internal grain-boundary network promotes redox activity within individual particles. Collectively, these results establish a multiscale design principle for iron-air anodes, in which electrode architecture governs electrolyte access, while grain-boundary engineering governs redox accessibility within the active material, providing complementary levers for maximizing iron utilization.

5. Experimental section

5.1. Materials and sample preparation

High purity iron foils (Sigma Aldrich, ≥99.99%, 0.25 mm thickness) were sectioned into 14 mm x 14 mm rectangular specimens. Grain size was tuned by vacuum annealing under ca. 10^{-6} mbar at 650 °C for 1 h for Fe01, 750 °C for 4 h for Fe20, and 1100 °C for 8 h for Fe2500. After heat treatment, all samples were subjected to the same surface preparation procedure: mechanical grinding with SiC papers from P1200 to P4000 grit, followed by polishing with 3 μm and 1 μm diamond suspensions, and final chemical mechanical polishing with colloidal silica (OPS). The final OPS step was used to remove residual near-surface deformation and obtain mirror-like surfaces suitable for EBSD analysis and subsequent electrochemical experiments. EBSD orientation maps and grain size distributions were collected before electrochemical testing to confirm the resulting microstructures.

5.2. Electrolyte preparation

The electrolyte was 6 M KOH, prepared by dissolving reagent grade KOH pellets (Sigma Aldrich) in deionized water. A 6 M solution corresponds to approximately 33.6% KOH by weight. Solutions were prepared and cooled to room temperature before use.

5.3. Microstructure characterization

Microstructures were examined using a Zeiss Merlin scanning electron microscope. Electron backscatter diffraction was performed in the same instrument equipped with an EDAX EBSD detector and operated using APEX software. Data processing and grain size analysis were conducted in EDAX OIM software (Version 9). Measurements were performed on OPS polished surfaces prior to electrochemical testing. Orientation maps confirmed fewer than ten boundaries within typical scan areas for the quasi-single-crystal, Fe2500 sample, equiaxed grains of about 20 μm in the Fe20 sample, and a dense network of approximately 1 μm grains in the fine-grained sample, Fe01.

The cross-sectional milling and the EDX measurement on the cycled samples were conducted on an FEI Helios Plasma dual beam scanning electron microscopy/focused ion beam (FIB) system with Xe ion source, equipped with and an EDAX EDX detector. TEM samples were prepared by ultrasonication and subsequent drop-cast on copper grids. TEM images and selected area diffraction patterns were recorded on a JEOL JEM-2100PLUS.

5.4. Electrochemical measurements

Electrochemical measurements were conducted in a three-electrode configuration using a custom Teflon cell. The working electrode was mounted in a PEEK holder with a circular aperture of 6 mm diameter (Redox.me), giving a geometric area of 0.283 cm^2. A platinum mesh served as the counter electrode, and a commercial reversible hydrogen electrode (HydroFlex RHE, Gaskatel) served as the reference electrode. The electrodes were positioned at identical distances inside a custom Teflon vessel for all the measurements. All measurements were

performed using a VSP-300 potentiostat operated with EC Lab software (BioLogic). Electrode spacing and immersion depth were kept constant across experiments.

5.5. Kinetic analysis

For a reversible one-electron process at 25 °C, the peak current is given by the classical expression in Eq (2).

$$i_p = 0.4463nFAC\left(\frac{nF\nu D}{RT}\right)^{1/2} \quad (2)$$

Where i_p is the peak current, n is the electron transfer number, F is the Faraday constant, A is the electrode area, C is the concentration of redox active sites, ν is the scan rate, D is the diffusion coefficient, R is the gas constant, and T is the temperature. Combining the factors of nF inside and outside the square root and collecting the thermodynamic constants gives the standard room temperature form, expressed in Eq (3) as:

$$i_p = 2.69 \times 10^5 n^{3/2} ACD^{1/2}\nu^{1/2} \quad (3)$$

Evaluating the apparent diffusivity in the system can be rationalized by isolating the diffusion coefficient, as shown in Eq (4).

$$D_{app} = \left[\frac{i_{diff}}{2.69 \times 10^5 n^{\frac{3}{2}} AC\sqrt{\nu}}\right]^2 \quad (4)$$

Here, n = 1 as the Fe(II) to Fe(III) transition proceeds through a one-electron mechanism in concentrated alkaline media [46]. $A = 0.283cm^2$ as the geometric electrode area determined from the circular aperture in the electrode holder. The concentration term was defined using the oxygen site density in α-FeOOH, which represents a structurally well-defined and widely used reference phase for iron oxyhydroxide redox chemistry [47–49]. Based on crystallographic data [49], the oxygen site concentration is C = 0.09299 mol O cm^{-3}.

The diffusion-controlled peak current was isolated using the mixed control expression shown in Eq (5), which is applied at the redox peak potential [38].

$$i(E,\nu) = k_1(E)\nu + k_2(E)\nu^{1/2} \quad (5)$$

Where k_1 and k_2 are the respective capacitive and diffusive contribution factors. Rearranging the terms as shown in Eq (6) allows for a straightforward extraction of both factors by regression of $i/\nu^{1/2}$ against $\nu^{1/2}$ through the slope and intercept.

$$\frac{i(E,\nu)}{\nu^{1/2}} = k_1(E)\nu^{1/2} + k_2(E) \quad (6)$$

The resulting coefficients were then used to obtain the diffusion-controlled current, i_{diff}, required in Eq (4), and are displayed in Table 1.

CRediT authorship contribution statement

Adam Cohen Miles: Writing – review & editing, Writing – original draft, Visualization, Validation, Methodology, Investigation, Formal analysis, Data curation, Conceptualization. **Yujun Zhao:** Writing – review & editing, Methodology, Investigation. **Dierk Raabe:** Writing – review & editing, Validation, Supervision, Project administration, Funding acquisition. **Yan Ma:** Writing – review & editing, Validation, Supervision, Project administration, Funding acquisition, Conceptualization. **Yug Joshi:** Writing – review & editing, Visualization, Validation, Supervision, Resources, Project administration, Methodology, Funding acquisition, Conceptualization.

Declaration of competing interest

The authors declare no competing interests.

Acknowledgements

The authors gratefully acknowledge Andreas Sturm, Christian Bross, Zakarya Meshou, and Volker Kree for their support to the FIB, SEM, Electrochemistry lab and TEM facilities at MPI-SusMat. A.C.M is grateful for funding from Horizon Europe Project HAlMan under grant agreement number 101091936. Y.J. is grateful for funding from EU Horizon Research and Innovation Actions under grant agreement number 101192848. Y.Z. acknowledges funding by the European Union through the EIC grant no. 101184347, Heat2Battery. DR. is grateful for the financial support through the ERC Advanced grant ROC (Grant Agreement No 101054368). Views and opinions expressed are, however, those of the author(s) only and do not necessarily reflect those of the European Union or the ERC. Neither the European Union nor the granting authority can be held responsible for them.

Supplementary materials

Supplementary material associated with this article can be found, in the online version, at doi:10.1016/j.ensm.2026.105409.

Data availability

Data will be made available on request.

References

[1] D.L. Cole, S. Dalvi, V.M. Zavala, O.J. Guerra, iScience 28 (2025) 112571.
[2] J. Twitchell, K. DeSomber, D. Bhatnagar, J. Energy Storage 60 (2023) 105787.
[3] K. Rodby, R. Jaffe, E. Olivetti, F. Brushett, K.E. Rodby, R.L. Jaffe, E.A. Olivetti, F. R. Brushett, J. Power Sources (2022), https://doi.org/10.26434/chemrxiv-2022-tnpsv.
[4] D. Reynard, C.R. Dennison, A. Battistel, H.H. Girault, J. Power Sources 390 (2018) 30–37.
[5] N. Poli, C. Bonaldo, M. Moretto, M. Guarnieri, Appl. Energy 362 (2024) 122954.
[6] K.E. Rodby, R.L. Jaffe, E.A. Olivetti, F.R. Brushett, J. Power Sources 560 (2023) 232605.
[7] L. Tang, H. Peng, J. Kang, H. Chen, M. Zhang, Y. Liu, D.H. Kim, Y. Liu, Z. Lin, Chem. Soc. Rev. 53 (2024) 4877–4925.
[8] W. Zheng, Y. Zhao, H. Zhang, L. Zhang, Z. Zhang, ACS Appl. Mater. Interfaces 16 (2024) 8885–8894.
[9] R.D. Al Bostami, A. Al Othman, M. Tawalbeh, A.G. Olabi, Energy Nexus 17 (2025) 100387.
[10] "Metal recycling factsheet by EuRIC European Circular Economy Stakeholder Platform," https://circulareconomy.europa.eu/platform/en/knowledge/metal-recycling-factsheet-euric, **n.d.**.
[11] B. Sun, H. Wang, C. Peng, Sustain. Energy Fuels 8 (2024) 5711–5730.
[12] M. Barman, M. Pal, R. Biswas, A. Dutta, Catal. Today 451 (2025) 115229.
[13] K. Bogomolov, Y. Ein-Eli, ChemSusChem 18 (2025) e202402412.
[14] M. Salado, E. Lizundia, Mater. Today Energy 28 (2022) 101064.
[15] Z. Li, J. Yu, X. Liu, ACS Appl. Energy Mater. 8 (2025) 9965–9982, https://doi.org/10.1021/acsaem.5c00946.
[16] P. Denholm, W. Cole, A.W. Frazier, K. Podkaminer, N. Blair, **n.d.**.
[17] P. Albertus, J.S. Manser, S. Litzelman, Joule 4 (2020) 21–32.
[18] A.A. Kebede, T. Kalogiannis, J. Van Mierlo, M. Berecibar, Renew. Sustain. Energy Rev. 159 (2022) 112213.
[19] W.H. Woodford, S. Burger, M. Ferrara, Y.M. Chiang, One Earth 5 (2022) 212–215.
[20] S. Sripad, D. Krishnamurthy, V. Viswanathan, OSF (2021), https://doi.org/10.1149/OSF.IO/A4SE8.
[21] M. Egashira, Encyclopedia of Electrochemical Power Sources, 2009, p. 372.
[22] R.D. McKerracher, C. Poncedeleon, R.G.A. Wills, A.A. Shah, F.C. Walsh, Chempluschem 80 (2015) 323–335.
[23] D.C. Lee, D. Lei, G. Yushin, ACS Energy Lett. 3 (2018) 794–801.
[24] M.A.R. Khollari, K.M. Deen, E. Asselin, NPJ Mater. Degrad. 9 (1) (2025) 119. *2025 9*.
[25] B.T. Hang, T.T. Anh, *Scientific Reports 2021 11:1* 2021, 11, 1.
[26] C. Fang, X. Tang, J. Wang, Q. Yi, Front. Energy 18 (2024) 42–53.
[27] B. Tian, J. Światowska, V. Maurice, S. Zanna, A. Seyeux, P. Marcus, Electrochim. Acta 259 (2018) 196–203.
[28] D. Mitra, A.S. Rajan, A. Irshad, S.R. Narayanan, J. Electrochem. Soc. 168 (2021) 030518.
[29] B.T. Hang, S.H. Yoon, S. Okada, J. Yamaki, J. Power Sources 168 (2007) 522–532.
[30] N. Villanueva, C. Alegre, J. Rubin, H.A. Figueredo-Rodríguez, R.D. McKerracher, C. P. De León, M.J. Lázaro, ACS Appl. Energy Mater. 5 (2022) 13439–13451.
[31] Q. Wang, C. Zhao, X. Hu, J. Wang, S. Ganapathy, S. Eustace, X. Bai, B. Li, H. Li, D. Aurbach, M. Wagemaker, J. Am. Chem. Soc. 146 (2024) 31778–31787.
[32] J. Hao, W. Wu, Q. Wang, D. Yan, G. Liu, S. Peng, J. Mater. Chem. Mater. 8 (2020) 7192–7196.

[33] X. Geng, M. Vega-Paredes, Z. Wang, C. Ophus, P. Lu, Y. Ma, S. Zhang, C. Scheu, C. H. Liebscher, B. Gault, Nat. Commun. 2024 15:1 15 (1) (2024).
[34] L. Zhang, X. Zhang, B. Guo, Z. Rong, Z. Yan, B. Wang, M. Li, Z. Wang, L. Zhu, Q. Huang, Y. Tang, J. Huang, ACS Energy Lett. 10 (2025) 898–906.
[35] M. Mead, N. Kerner, R. Talei, Y. Joshi, G. Schmitz, 2025, doi 10.2139/SSRN.5763143.
[36] N.A. Sepulveda, J.D. Jenkins, A. Edington, D.S. Mallapragada, R.K. Lester, Nat. Energy 6 (2021) 506.
[37] M.K. Nieuwoudt, J.D. Comins, I. Cukrowski, J. Raman Spectrosc. 42 (2011) 1353–1365.
[38] J. Wang, J. Polleux, J. Lim, B. Dunn, J. Phys. Chem. C 111 (2007) 14925–14931.
[39] H. Lindström, S. Södergren, A. Solbrand, H. Rensmo, J. Hjelm, A. Hagfeldt, S. E. Lindquist, J. Phys. Chem. B 101 (1997) 7717–7722.
[40] K. Aoki, K. Tokuda, H. Matsuda, J. Electroanal. Chem. Interfacial Electrochem. 146 (1983) 417–424.
[41] J. Mürter, S. Nowak, E. Hadjixenophontos, Y. Joshi, G. Schmitz, Nano Energy 43 (2018) 340.
[42] J.E.B. Randles, Trans. Faraday Soc. 44 (1948) 327–338.
[43] K.J. Gallagher, D.N. Phillips, Trans. Faraday Soc. 64 (1968) 785–795.
[44] J. Takada, S. Yamamoto, S. Kikuchi, M. Adachi, Oxid. Met. 25 (1986) 93–105.
[45] M. Sander, T.B. Hofstetter, C.A. Gorski, Env. Sci. Technol. 49 (2015) 5862–5878.
[46] S. Fen Tan, H. Wu, J.S. Manser, D. Zhang, M. Ronchi, S. Smullin, Y.-M. Chiang, F. M. Ross, S.F. Tan, H. Wu, D. Zhang, Y.-M. Chiang, F.M. Ross, J.S. Manser, M. Ronchi, S. Smullin, Adv. Funct. Mater. 35 (2025) 2407561.
[47] A. Jiménez-Vázquez, R. Jaimes-López, C.M. Morales-Bautista, S. Pérez-Rodríguez, Y. Gochi-Ponce, L.A. Estudillo-Wong, Catalysts 15 (2025) 236.
[48] L. Notini, D.E. Latta, A. Neumann, C.I. Pearce, M. Sassi, A.T. N'Diaye, K.M. Rosso, M.M. Scherer, Env. Sci. Technol. 52 (2018) 2751–2759.
[49] R.M. Cornell, U. Schwertmann, *The Iron Oxides: Structure, Properties, Reactions, Occurences and Uses*, 2004.